Drag reduction in fish-like locomotion

By D. S. BARRETT[1], M. S. TRIANTAFYLLOU[1]†,
D. K. P. YUE[1], M. A. GROSENBAUGH[2]
AND M. J. WOLFGANG[1]

[1]Department of Ocean Engineering, Massachusetts Institute of Technology,
Cambridge, MA 02139, USA
[2]Department of Applied Ocean Physics and Engineering, Woods Hole Oceanographic Institution,
Woods Hole, MA 02543, USA

We present experimental force and power measurements demonstrating that the power required to propel an actively swimming, streamlined, fish-like body is significantly smaller than the power needed to tow the body straight and rigid at the same speed U. The data have been obtained through accurate force and motion measurements on a laboratory fish-like robotic mechanism, 1.2 m long, covered with a flexible skin and equipped with a tail fin, at Reynolds numbers up to 10^6, with turbulence stimulation. The lateral motion of the body is in the form of a travelling wave with wavelength λ and varying amplitude along the length, smoothly increasing from the front to the tail end. A parametric investigation shows sensitivity of drag reduction to the non-dimensional frequency (Strouhal number), amplitude of body oscillation and wavelength λ, and angle of attack and phase angle of the tail fin. A necessary condition for drag reduction is that the phase speed of the body wave be greater than the forward speed U. Power estimates using an inviscid numerical scheme compare favourably with the experimental data. The method employs a boundary-integral method for arbitrary flexible body geometry and motions, while the wake shed from the fish-like form is modelled by an evolving desingularized dipole sheet.

1. Introduction

Recent work has shown that unsteady motion of a body offers possibilities for efficient flow control (Ffowcs Williams & Zhao 1989; Tokomaru & Dimotakis 1991). Similarly, unsteady propulsion offers certain advantages not present in conventional steady propulsors. It has been shown, for example, that unsteady motion of airfoils causes very high lift coefficient (Gursul & Ho 1992), and can produce propulsive thrust very efficiently (Triantafyllou, Triantafyllou & Grosenbaugh 1993; Anderson *et al.* 1998). Also, an oscillating foil can be used to alter and reposition oncoming vorticity (Koochesfahani & Dimotakis 1988) and to recapture energy contained in the eddies of an oncoming flow using vorticity control (Gopalkrishnan *et al.* 1994).

The effects of periodic forcing of a flow have been studied by several investigators. Roberts & Roshko (1985) showed that the vortex structure and mixing can be influenced by pulsing the flow. Taneda (1978) showed that the wake width behind a cylinder placed within an oncoming stream can be reduced by imposing harmonic rotary oscillations. Tokomaru & Dimotakis (1991) considered the same problem in

† Author to whom correspondence should be addressed.

detail and found that rotary oscillation exerts a maximum influence on the flow when the frequency is close to the Strouhal frequency. Under proper conditions the wake width, and hence drag, can be reduced substantially. They also make the point that in unforced wakes the separation points move relatively little, and the natural instability of the flow redistributes the vorticity to create the large-scale patterns, whereas in a forced oscillation the separation points move substantially, hence gathering vorticity near the cylinder and releasing it in the wake. Taneda & Tomonari (1974) considered the effect of imposing a travelling wave motion on the flow around a flexible plate placed in a stream of velocity U. He showed that when the speed of propagation of the travelling wave c_p exceeds the free-stream velocity, turbulence in the boundary layer of the plate is suppressed.

Fish swimming can be very instructive in exploring mechanisms of unsteady flow control because it has developed as a result of many millions of years of evolutionary optimization. Seminal contributions by Lighthill (1975) and Wu (1961, 1971) have shed light on the inviscid hydromechanics of fish-like propulsion, while predicting high propulsive efficiency. Reported outstanding performance by fish (Aleyev 1977; Harper & Blake 1990) has led to increased interest in fish-like vehicles capable of emulating the high performance of fish propulsion and manoeuvring. The question we address herein is whether unsteady flow control can also lead to overall drag reduction in streamlined bodies, a task that has proved elusive so far.

This question was actually raised first in relation to swimming of live fish. Gray (1936) compared the power required by a rigid model of a dolphin to move at speeds around 20 knots with its estimated available muscular power. He estimated that the available muscular power is smaller than the power required to propel the rigid model by a factor of seven (*Gray's paradox*), thus concluding that substantial drag reduction must occur in the live dolphin. Gray's conclusions have remained controversial for over sixty years largely because it is extremely difficult to obtain reliable force measurements from live fish. Recent work by Rome, Swank & Corda (1993) has outlined a methodology that may provide in the near future a definitive answer based on live fish measurements.

The development of a robotic mechanism, which can emulate very closely the swimming of the tuna (Barrett & Triantafyllou 1995; Triantafyllou & Triantafyllou 1995), overcomes the difficulties associated with live fish, because it allows the acquisition of detailed accurate measurements of the hydrodynamic forces on an actively controlled flexible body swimming like a fish. Repeated precise measurements on the flexible robot have shown that, within a parametric range, drag in an actively swimming vehicle at Reynolds number of about 10^6 can be reduced by 50% or more (up to 70% within the range considered), compared with the value on the same vehicle towed in a rigid–straight configuration. This drag reduction can be attributed only to the effect on the flow of the imposed body flexing in the form of a travelling wave.

In the absence of significant flow separation, inviscid methods employing a Kutta condition at all trailing edges and including proper modelling of the self-induced wake dynamics are expected to provide reasonable estimates of the power needed by the fish-like body once the kinematics are specified. To prove this hypothesis and hence shed additional light on the governing flow mechanisms, we developed an inviscid numerical scheme employing a boundary integral formulation for arbitrary body geometry and imposed motions, with desingularized infinitesimal wake sheet representation to model the nonlinear dynamics of the wake vorticity. This numerical model has been validated through systematic convergence tests. The numerical model is found to compare well with the experimental robotic fish data for the power expended by the motors.
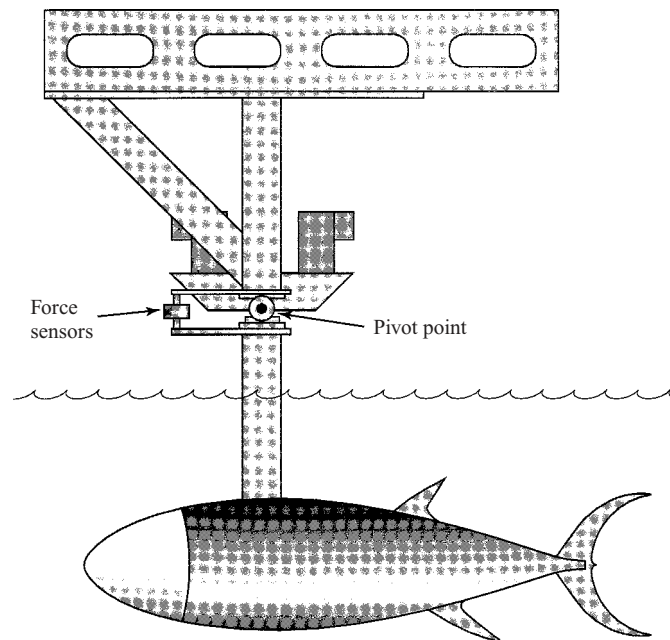
FIGURE 1. Lateral view of the robotic fish-like mechanism and the supporting structure attaching it to the overhead carriage.

2. Experimental apparatus

The robotic mechanism has length $L = 1.25$ m and consists of a streamlined main body capable of flexing and a propulsive tail fin. The outer shape of the vehicle in its position at rest is an exact replica of the shape of a bluefin tuna (*thunnus thynnus*), including the caudal and two smaller attached fins. The mechanism was tested in the Ocean Engineering Testing Tank Facility at MIT in a water tank with dimensions 35 m long by 2.5 m wide by 1.25 m deep. The robot is connected to an overhead carriage through a streamlined strut so it can be towed at constant speed, as shown in figure 1. It was towed at mid-depth to avoid interference effects with the free surface and the bottom.

The cross-section of the body closely resembles an ellipse; the maximum transverse dimensions are found at mid-length: height 0.30 m and width 0.21 m. The caudal fin has maximum (vertical) span 0.32 m. The mechanism is a high-precision assembly of eight links made of anodized aluminium and covered with a special skin structure. A schematic description of the robotic mechanism can be found in Barrett & Triantafyllou (1995), Triantafyllou & Triantafyllou (1995), and Barrett (1996), while figure 2 provides the basic outline of the mechanism, consisting of eight sequential rigid links, each capable of relative rotation with respect to its neighbouring links. Elliptical bulkheads define the outer hull shape, while triangulated space frames provide the required rigidity for transmitting large forces and for supporting the skin structure (figure 2). Hull flexing is accomplished through activation of the links by six brushless motors, 3 hp each, mounted on the towing carriage. There are six degrees of freedom since the second link is rigidly attached to the carriage, while the first and third links are coupled to move in anti-phase. The remaining five links are independently controlled. An assembly of strings and pulleys transmits the motion to individual links with minimal frictional forces as shown in figures 3, 4, and 5: there is a pair
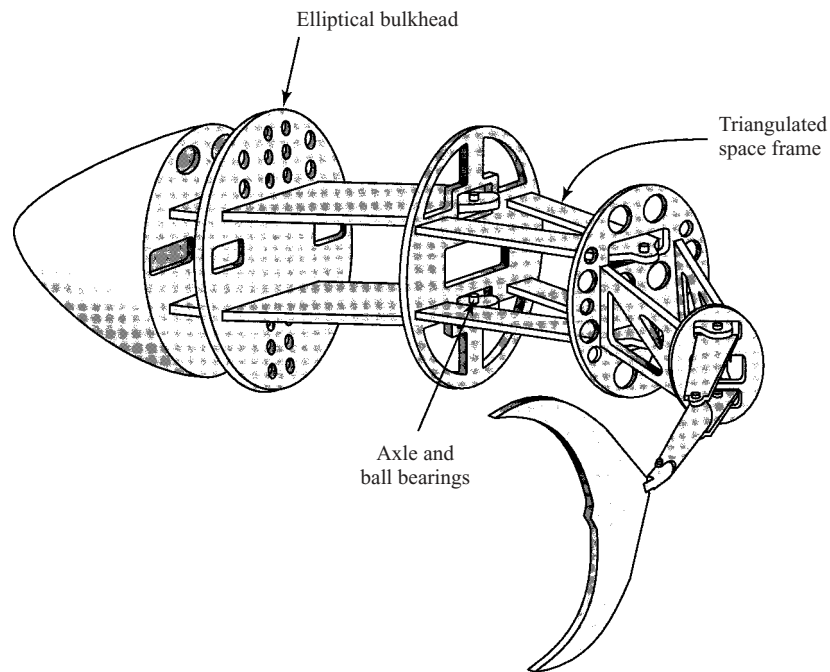
FIGURE 2. Schematic view of the eight internal links of the robotic mechanism.
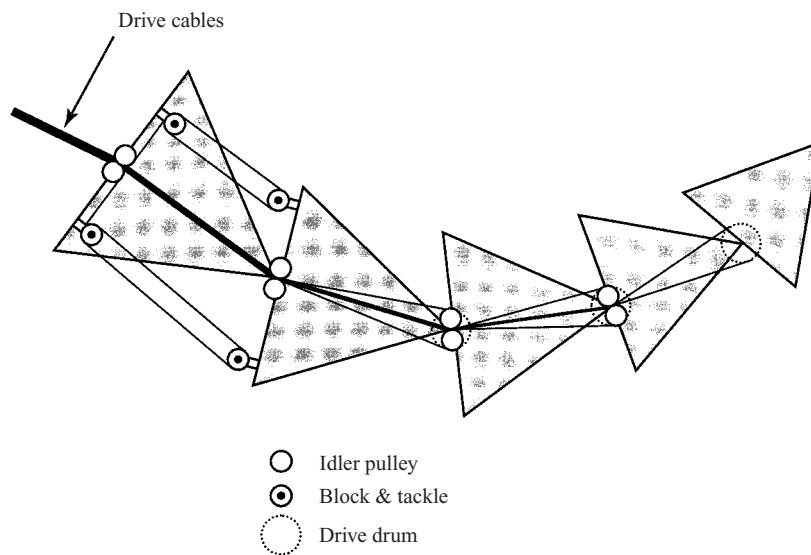

FIGURE 3. Actuation mechanisms of relative rotations of the posterior five robotic links.

of activating cables per motor, one pulling in and the other reeling out. All six pairs of cables run through the vertical strut and are guided by idler pulleys to reach the specific link they will activate.

Figure 4 shows the activation of a midbody link, where ample space is available for generating a large torque: the corresponding pair of cables reach the near-end of the link and are deflected by idler pulleys outwards and in opposite directions,
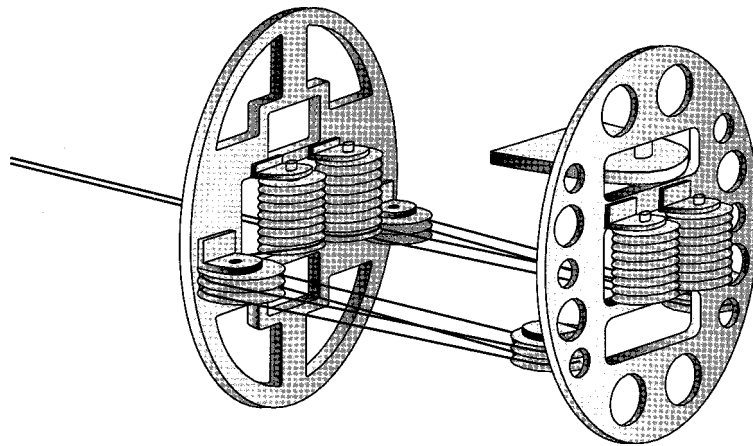
FIGURE 4. Block and tackle arrangement used for transmission of rotational motion through pulleys and cables to midbody bulkheads.
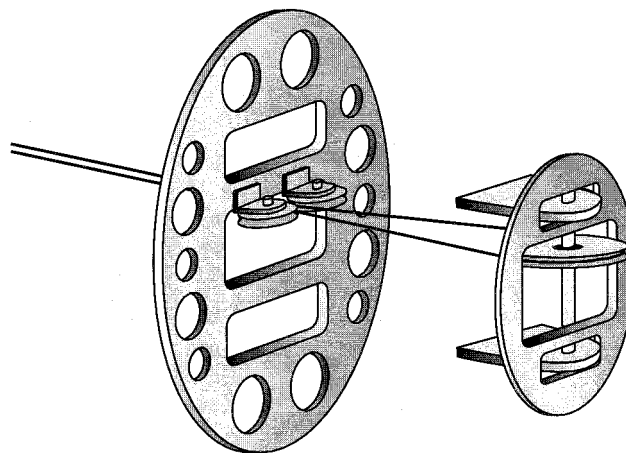

FIGURE 5. Drive drum arrangement used for transmission of rotational motion through pulleys and cables to afterbody bulkheads.

wrap around pulleys located at the ends of the bulkhead, and then run across and reach pulleys at the bulkhead lying at the farthest-end of the link (block and tackle arrangement). By pulling-in one cable and reeling-out the other a relative rotation is achieved at high torque.

Figure 5 shows the activation of the three last links closest to the tail, where space is restricted: the corresponding pair of cables reach the near-end of the link and are deflected slightly outwards to reach a large pulley at the next bulkhead, around which both wires wrap around (drive drum arrangement). By pulling-in one cable and reeling-out the other a relative rotation is achieved.

Figure 6 is a colour photograph of the actual robotic mechanism, showing the eight links in a deflected state and providing details of the schematic arrangements of figures 2 and 3.

As explained above, the second link is fixed to the strut and the first and third links are coupled to move in anti-phase; hence only six links are independently activated, one for each motor. The idler pulley arrangement causes nearly complete decoupling
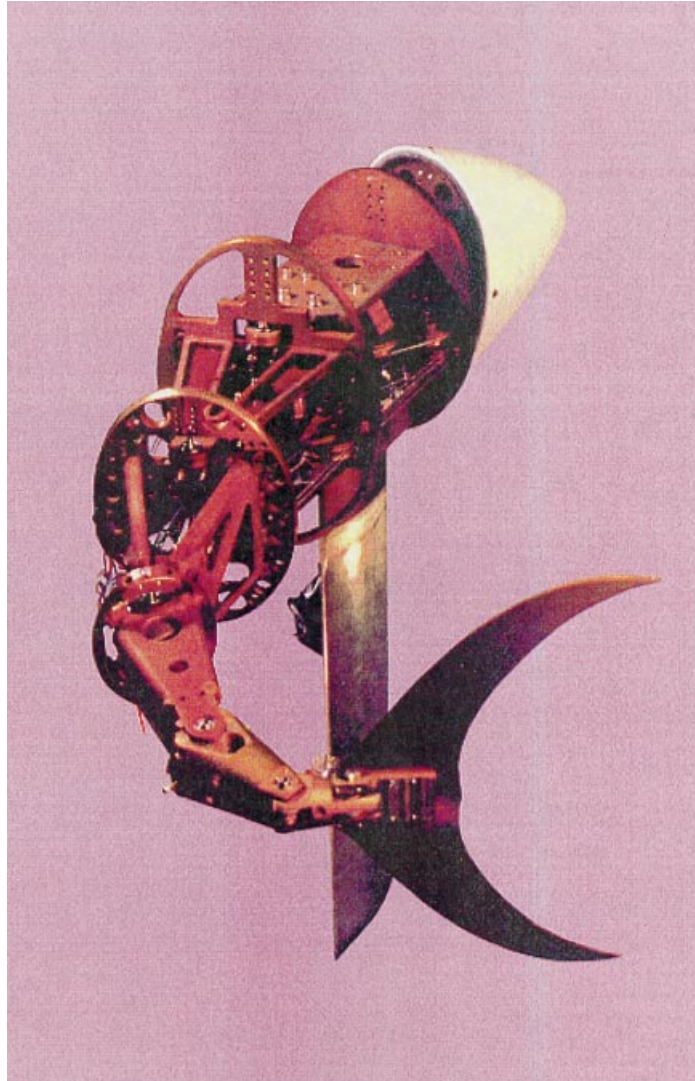
FIGURE 6. Photograph depicting the eight body links. Strut (mast) and body are upside down.

in the actuation of each degree of freedom; and since each degree corresponds physically to the actuation of one joint between links we will refer to six *joints*, numbered sequentially from the front joint 0 (activating the coupled first and third links) to the tail joint 5 (activating the tail fin).

To allow smooth flexing of the external surface, a structure was developed consisting of a set of densely packed plastic ribs, fixed transversely on stainless steel backbones running between the ends of adjacent links and each providing a wide support area for the skin to rest on. A special impermeable skin structure was employed, one inch thick, consisting of layers of filter foam and tensioned thin latex sheets, contained on both sides inside a conformal Lycra skin and supported by reticulated foam.

Strain-gauge-based miniature load cells (*Entran elf-tc500*) are mounted on each of the twelve actuating strings (two strings per motor), while displacement sensors (*ETI servomount precision potentiometers*) provide motion measurements, thus allowing a
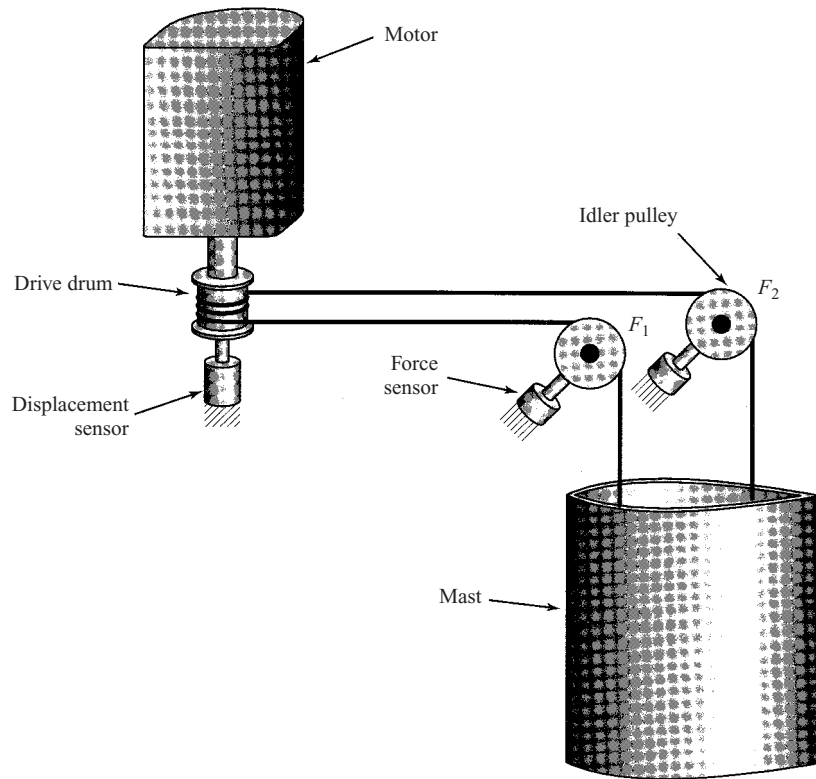
FIGURE 7. Force and displacement transducers for each of the six motors.

complete evaluation of the power required to drive the mechanism (figure 7). The transducers are mounted near the driving motors so as to be easily accessible for frequent inspection and calibration; no drift was observed during testing. The drag or thrust on the overall mechanism is measured by two force transducers (figure 1), a load cell (*Entran elf-tc1000*) and a Kistler quartz force transducer, for redundancy.

The motion was initially selected to resemble the tuna motions observed in live tuna (Fierstine & Walters 1968), but variations were also introduced to investigate the effect of the shape parameters. The motion was curve-fitted so as to be purely sinusoidal and to consist of a smooth amplitude-modulated travelling wave along the length with constant phase speed, $c_p = \omega/k$, which may in general differ from the swimming speed U. The imposed transverse motion $y(x,t)$, in a body-fixed coordinate system with x measured starting from the edge of the second link and positive towards the tail, has the form

$$y(x,t) = a(x)\sin(kx - \omega t), \tag{2.1}$$

where $k = 2\pi/\lambda$ is the wavenumber, corresponding to wavelength λ, ω is the circular frequency of oscillation, and $a(x)$ is the amplitude envelope, given as

$$a(x) = c_1 x + c_2 x^2, \tag{2.2}$$

where c_1 and c_2 are adjustable parameters. We chose c_1 to be independent, while c_2 is chosen to achieve a specific value of the double-amplitude of motion, denoted by A, at the tail. The distance x is measured from the edge of the second link, which is rigidly attached to the towing strut, positive towards the tail, and is non-dimensionalized

by the body length. Typically, the phase speed $c_p = \omega/k$ is larger than the forward speed U, while the wavelength λ is close in value to the body length. The frequency scaling of data observed in fish is based on the wake Strouhal law (Triantafyllou, Triantafyllou & Gopalkrishnan 1991; Triantafyllou *et al.* 1993), i.e. keeping constant the non-dimensional parameter St:

$$St = fA/U, \qquad (2.3)$$

where f is the frequency of oscillation and A is the average total lateral excursion of the tail fin at its junction to the body.

Each run is conducted as follows: an initial force measurement is taken with the mechanism at rest to obtain a zero force measurement; then the motors impose a travelling wave motion, and after a few seconds, the towing carriage starts and enforces a constant speed until the apparatus reaches near the end of the tank when the carriage and motors stop and a second zero force measurement is taken. Throughout the run we measure and record the instantaneous forces and movement of the actuating strings, as well as the overall force on the carriage.

3. Calibration and testing of force and displacement sensors

The apparatus was calibrated and evaluated by imposing known (*a*) external static loads and (*b*) dynamic loads in the form of weights lifted through pulleys, to ensure that force and power measurements are accurate. Since force and motion data are obtained near the motors (figure 7), conservative power estimates are calculated, which include frictional losses in the strings and pulleys and in the moving parts of the main body of the mechanism.

The dynamic tests to evaluate the accuracy of measurements were conducted using the following apparatus, which we will call the *dynamic calibration apparatus*: a flexible string was attached at the centre of the trailing edge of the tail fin. This line passes through a low-friction idler pulley located at a distance of 0.50 m off to the side of the mechanism. The pulley bends the string which leaves vertically up through the water surface, and its end is attached to a load cell identical to the ones used in the mechanism to measure cable forces. A string connects the other end of the load cell though a second idler pulley to a hanging weight. The second pulley is connected to a precision multi-turn potentiometer, identical to the ones used in the mechanism to measure cable displacement.

The tests were conducted as follows: each link individually was commanded to move a certain amount of encoder counts, first in a clockwise direction and then in the opposite direction, for example $\pm 5°$. This resulted in motion of the tail and hence, through the apparatus described, to motion of the hanging weight, which was measured through the motor potentiometer (motor motion). The same displacement was calculated using the potentiometers fitted on the strings of the mechanism (measured motion). Testing provided the results shown in table 1. It should be noted that flexibility of the mechanism and the strings account partly for the deviation shown, while results represent a worse-case scenario, since motions are imposed at the extreme end of the mechanism (the tail) and errors in the intermediate links are cumulative.

Subsequently, known weights were hung from the dynamic calibration apparatus. Sequentially, the force transducers near the motors were used to measure the force on the cables and hence deduce the force acting on the tail. The force transducers were previously calibrated by hanging weights directly on the actuating cables near the

Segment no.	Commanded motion (deg.)	Distance link-tail (m)	Motor motion (m)	Measured motion (m)	Difference (%)
0	± 5	0.610	0.1058	0.1018	4.1
1	± 5	0.432	0.0753	0.0720	4.3
2	± 5	0.279	0.0487	0.0494	-1.5
3	± 5	0.152	0.0529	0.0499	5.6
4	± 10	0.0762	0.0264	0.0272	2.9
5	± 30	0.0508	0.0508	0.0529	4.0

TABLE 1. Evaluation of imposed motion accuracy.

Segment no.	Transmission ratio	Weight (N)	Applied force (N)	Measured force (N)	Difference (%)
0	2.283	4.448	10.16	9.61	5.4
1	2.461	4.448	10.95	9.95	9.1
2	11.15	4.448	49.62	46.34	6.6
3	8.817	4.448	39.21	35.85	8.5
4	7.142	4.448	31.77	30.37	4.6
5	6.193	4.448	27.54	27.10	1.5

TABLE 2. Evaluation of external force measurement accuracy.

motors shown in figure 7. Table 2 provides the results; the transmission ratio, used to correlate the force applied at the tail with force measurements on the activating cables, is calculated using the distance of the link to the tail and the type of activation mechanism used (the two types of activation are shown in figures 4 and 5). The applied force is obtained by multiplying the known weight by the transmission ratio, while the measured force is the value provided by the cable transducers. The deviation reflects the flexibility of the mechanism as well as measurement errors, while static-frictional forces result consistently in measured forces which are smaller than the actual applied forces.

Next, weights were hung from the calibration mechanism and each link of the mechanism was commanded, separately, to move a certain distance at slow speed. The energy needed to execute the commanded motion was calculated in two ways: (*a*) the power used by the motors was integrated over the time interval of the experiment (motor energy); (*b*) the known weight and the motion measurements of the calibration apparatus were used to calculate the potential energy change (measured energy). Table 3 summarizes the results. It should be noted that the internal losses in the mechanism result in higher motor energy than measured energy; these internal losses become progressively smaller as the measurements are made closer to the point of force application (i.e. near the tail). Hence these error estimates represent an upper bound, particularly for the links further away from the tail, since in the swimming experiments fluid forces are distributed along the entire body.

Finally, weights were hung from the calibration mechanism and each link of the mechanism, separately, was commanded to move in an oscillatory motion of constant amplitude; and at frequency 1 Hz, which is representative of the frequencies used in the experiments reported in this paper. The energy needed to execute the commanded oscillatory motion was calculated in two ways: (*a*) the power used by the motors was averaged over 10 cycles, after the initial transients had died down and steady state was obtained (motor power); (*b*) the force and motion transducers of the dynamic

Segment no.	Motor energy (J)	Measured energy (J)	Difference (%)
0	0.169	0.148	12.4
1	0.180	0.155	13.9
2	0.181	0.160	11.6
3	0.167	0.153	8.3
4	0.154	0.147	4.5
5	0.159	0.151	5.0

TABLE 3. Evaluation of energy measurement accuracy at low frequency.

Segment no.	Motor power (W)	Measured power (W)	Difference (%)
0	0.184	0.158	14.1
1	0.179	0.153	14.5
2	0.175	0.154	12.0
3	0.170	0.159	6.5
4	0.151	0.143	5.3
5	0.164	0.154	6.1

TABLE 4. Evaluation of power measurement accuracy at high frequency.

calibration apparatus were used to calculate the average power over the same time interval as with the motor power measurement (measured power). Table 4 summarizes the results. Again, the internal losses in the mechanism result in higher motor power; these losses become progressively smaller as the measurements are done closer to the point of force application.

A considerable effort was expended trying to minimize hysteretic and other losses in the mechanism. The external force and dynamic calibration tests are extreme cases in that the force is concentrated at a point, and the links further away from the applied force are subject to cumulative hysteretic losses and effects from the flexibility of the mechanism. Also, the errors include measurement errors twice, i.e. in the dynamic calibration mechanism transducers (which are absent during actual testing), as well as the motor transducers. We estimate on the basis of the experiments we conducted that power losses of the order of 5% (i.e. similar to the errors found from the dynamic calibration mechanism in the links near the tail) are more representative for the overall actively swimming mechanism.

4. Force and power measurements

We obtained an upper bound estimate of the flapping mechanism drag based on experimental force and power measurements. First, we outline the conventional definition of propulsive efficiency and then show how this can be used to calculate a conservative estimate of drag reduction.

4.1. *Conventional definition of propulsive efficiency*

In conventional marine propulsion studies, where a large rigid body is fitted, usually at its stern, with a propulsor of relatively small dimensions, it is possible to directly measure the thrust T developed by the propulsor by placing a force transducer at the connection between the body and the propulsor. The system propulsive efficiency η_p,

when moving at constant forward velocity U, is defined as

$$\eta_p = \frac{P_E}{P_p}, \tag{4.1}$$

where $P_E = U\,T_A$ is the useful power, T_A denotes the time-averaged thrust T, and P_p is the time-averaged power expended by the motors to drive the propulsor.

Hence, in a specific application we can use the directly measured thrust T and the power supplied by the motors to calculate the propulsive efficiency using (4.1).

By conservation of energy, the average power provided by the motors, P_p, can be further written as the sum of the useful power P_E and power losses P_l and P_w:

$$P_p = P_l + P_E + P_w, \tag{4.2}$$

where all quantities are time-averaged; P_l denotes the transmission losses from the motors to the propulsor; P_w denotes the energy wasted in the wake (such as, among other components, the rotational energy imparted to the fluid by a screw propeller).

For a self-propelled body the time-averaged drag D_A is equal to the time-averaged propulsor thrust T_A, hence measuring the thrust provides the value of the drag force as well. Note that herein the drag force is defined positive when pointing against the direction of forward motion, while all other axial forces (thrust, mast force) are positive when pointing in the direction of forward motion.

Despite the possibility of measuring thrust in conventional propulsion, interference effects still exist since the propulsor alters the pressure in the stern, while it operates within the ship wake. These phenomena are accounted for in ship model testing through the thrust deduction and wake fraction factors.

4.2. *Drag reduction in a flapping mechanism*

In the case of the present mechanism the propulsor cannot be distinguished from the body, because the motor power is supplied to several actively controlled links throughout the body length. Hence, a measurement of the propulsor thrust is impossible since there is no distinct interface between a separate body and a propulsor. As a result, neither the propulsive efficiency nor the drag D of an actively swimming body may be measured. The axial force measured at the strut (mast) of the present mechanism, F_n, is the x-component of the net fluid and body force acting on the overall mechanism and would correspond in the case of a conventionally propelled body to the difference between the thrust and the drag forces; for a self-propelled body, the time-averaged net axial force F_A is equal to zero.

The only directly measurable quantity is the average power supplied by the motors for self-propulsion, P_p. Hence, the only propulsive efficiency assessment that can be made is comparative, i.e. we can compare the power consumed to self-propel an actively swimming body with the power required to tow it rigidly at the same speed (or with the power required by a different propulsor to propel the same body). *Drag reduction in an actively swimming mechanism is defined in this study to occur when the net power supplied by the motors for self-propulsion is less than the power to tow the rigid body at the same speed.*

In order to obtain quantitative estimates of drag reduction, we proceed to find an *upper-bound estimate* of the drag on an actively swimming, self-propelled body moving at steady speed U as follows: first, by conservation of energy the net power supplied by the motors, P_p, can be subdivided as in (4.2), i.e. $P_p = P_l + P_E + P_w$; where P_l is again transmission losses, P_w is the power wasted in the wake, and $P_E = T_A\,U$ is the propulsive power, equal to the averaged propulsive thrust T_A times

the forward velocity U. For a self-propelled mechanism the averaged thrust must equal the averaged drag, $T_A = D_A$. Hence, we find the following inequalities for a self-propelled body:

$$P_E \leqslant P_p, \tag{4.3}$$

$$P_E = T_A U = D_A U, \tag{4.4}$$

$$D_A \leqslant P_p / U. \tag{4.5}$$

If the mechanism is not self-propelled, then it is producing a net axial force, which in the present experiments we measure as the mast force F_n. Then, one substitutes $T_A = F_A + D_A$, where F_A is the time average of the mast force, to find for a net-force-producing mechanism, forced to move at constant speed U:

$$D_A \leqslant D_u, \tag{4.6}$$

$$D_u = P_p / U - F_A, \tag{4.7}$$

where D_u is the upper-bound estimate of the drag force. A self-propelled body provides zero average mast force F_A and then (4.7) reverts to (4.5).

It should be noted that the actual value of the thrust and drag forces cannot be determined; the upper-bound estimate of the drag force is easily obtainable, however, in terms of two directly measurable quantities, P_p and F_A. If D_o is the drag of the body towed rigid at the same speed, we define drag reduction to occur when

$$D_u \leqslant D_o \tag{4.8}$$

and we quantify the drag reduction by the ratio

$$(D_o - D_u)/D_o. \tag{4.9}$$

Criterion (4.8) is conservative, hence the utility of D_u as a gauge of drag reduction depends on having small transmission losses and high hydrodynamic efficiency, so that the upper-bound drag estimate be close to the actual drag value. As a result, every effort was expended when designing the present mechanism to minimize frictional and material losses, while an extensive study was needed to identify parametric values of maximum drag reduction.

Finally, because axial force measurements include the drag of the mast and appendages, such as the tail and two small fins, as well as interaction drag, a simpler criterion was developed and used as an auxiliary means for assessing drag reduction. The following ratio, I_p, is called the *propulsive index*:

$$I_p = \frac{(D_o + F_A)U}{P_p}. \tag{4.10}$$

If I_p is greater than 1, i.e. if

$$I_p > 1 \tag{4.11}$$

then there must be drag reduction, $D_A \leqslant D_o$, otherwise energy conservation would be violated. This is easy to show, since by conservation of energy $(D_A + F_A)U \leqslant P_p$.

The propulsive index is a useful (but conservative) criterion because it is easy to construct: one needs only to add the measured rigid body drag D_o to the average measured mast force during active swimming F_A, without first subtracting from either measurement the correction drag (mast drag and other appendage drag). Indeed, if D_c denotes the correction drag, then in the rigid body case we measure a drag force

equal to the body drag plus D_c, while in the active swimming case we measure a mast force equal to the body force minus D_c (by virtue of the fact, as pointed out above, that drag and mast force are positive in opposite directions); when the two are added, D_c is eliminated.

4.3. *Calculation of the flapping body drag and power*

The calculation of an upper bound of the flapping body drag, D_u, is based on (4.7), involving two quantities: the measured mast force F_A; and the motor power P_p, which is found using the force and motion data of the string actuators as described in the following.

Two strings are connected to each motor, resulting in a total of twelve strings. For the jth motor the first string is pulled in (paid out) with velocity V_j while registering force F_{1j}, and the second string is paid out (pulled in) with equal velocity V_j while registering force F_{2j}. The forces represent the tensions measured on the string and are always positive; hence the net input power from the jth motor is $P_j = F_{1j}V_j - F_{2j}V_j = (F_{1j} - F_{2j})V_j$. We define the jth joint force as $F_j = F_{1j} - F_{2j}$ and then the instantaneous input power is found as $P_j = F_jV_j$. The overall instantaneous power is calculated as the sum of the input power in all six joints and then integrated to find the average power absorbed. An average over several cycles was calculated after steady state was achieved.

The mast force, as measured in the present set of experiments, i.e. at the top of the mast, contains the drag of the strut (mast) including some wave-making drag at the free surface, the interaction drag between the flexible mechanism and the mast, and the drag of the mechanism including the attached fins and the tail. As explained above, the criterion for drag reduction (4.11) does not require a correction for these quantities. In order, however, to obtain estimates of the drag coefficient on the body alone, the drag of these components (correction drag) must be measured and then used to correct the measured axial force. For this reason, we measured experimentally, as function of speed: (*a*) the mast drag with the body removed, replaced by a flow fairing, and (*b*) the tail drag separately; and thus obtained the net drag on the fish-like body of the mechanism. We did not correct for: (*a*) interference drag which was expected to be more important for the mast–body and body–tail interactions; and (*b*) the presence of the two smaller fins.

4.4. *Experimental results*

The experimental results have proved to be both reliable and repeatable. Figure 8 (Beal 1999) shows the mean power input to each joint averaged over a number of swimming cycles under conditions of self-propulsion for five distinct trial runs. The mean power standard deviation at each joint is small, with a 0.6% standard deviation from the mean total joint power of 0.5283 W.

As an example, figure 9 shows the measured motions of the six joints as function of time, for the following parametric values: speed $U = 0.7\,\mathrm{m\,s^{-1}}$ corresponding to Reynolds number based on the body length $Re = UL/v = 800\,000$; double amplitude (peak to peak) of the excursion of the attachment point of the tail $A = 0.16\,\mathrm{m}$; and frequency $f = 1.1\,\mathrm{Hz}$, resulting in Strouhal number $St = 0.25$. The body motion wavelength was $\lambda = 1.06\,\mathrm{m}$, providing $c_p/U = 1.67$. The phase angle between the lateral motion of the tail at the attachment point and angular motion was $90°$; the pitch angle was selected such that the maximum nominal angle of attack of the tail fin was $14°$.

As seen in figure 9, there is an initial ramp-up time period when joint motions
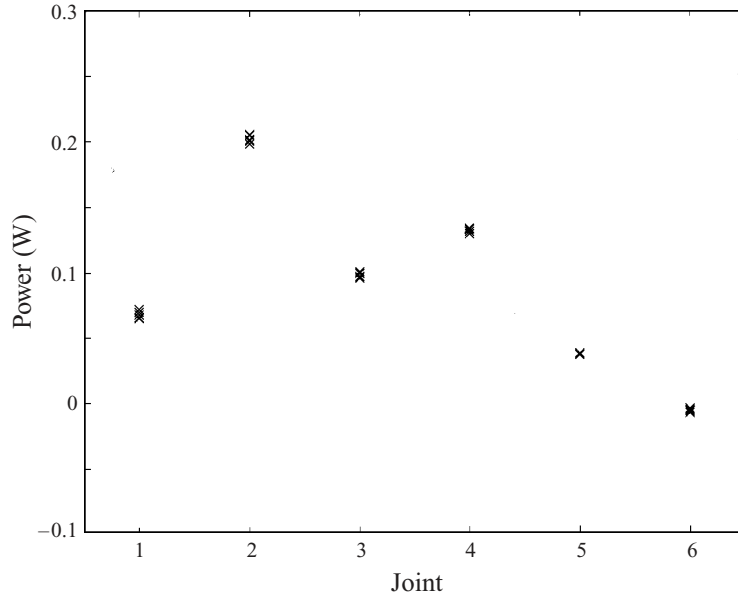
FIGURE 8. Mean power input to each joint under conditions of self-propulsion repeated over five trials. Mean total power input is 0.5283 W with a standard deviation of 0.0032 W (0.6%). Non-dimensional parameters: $St = 0.156$, $Re = 800\,000$. Run parameters: $U = 0.7\,\mathrm{m\,s^{-1}}$, $A = 0.108\,\mathrm{m}$, $f = 1.0\,\mathrm{Hz}$, $\lambda = 1.36\,\mathrm{m}$. Taken from Beal (1999).

are gradually imposed, eventually reaching a steady-state condition. The difference in amplitude and the time lag between the motions of subsequent joints are evident from the figure, corresponding to a travelling wave of increasing amplitude towards the tail. Self-propulsion conditions are assessed after the motions have achieved several periods of steady-state behaviour. Although efforts to minimize the static and dynamic friction and the external vibrations between the eight sets of rubber wheels and the rail support have resulted in an optimal low-friction configuration, the weight of the overhead carriage of about 600 pounds and the significant stiffness of the carriage drive belt, driven by a 5 hp motor with motion feedback, minimize the effect of unsteady forces on the motion of the carriage, which is steady at speed U typically within 2%. The measured unsteady axial forces from the mechanism are below 4 pounds at a frequency around 1 Hz.

Figure 10 shows for each of the six joints the measured forces and velocities after steady-state conditions have been established. The measured total average power in the example case was $P_F = 1.83\,\mathrm{W}$ and the net average thrust $T_A = 1.66\,\mathrm{N}$. The drag of the rigid system at the same speed was measured to be $D_o = 1.73\,\mathrm{N}$, including the drag of the appendages, which include the submerged part of the mast, the tail fin and two smaller fins attached on the body, as well as interaction drag. First we use the propulsive index, (4.10), which does not require subtraction of a correction drag: we find that $(T_A + D_o)U = 2.37\,\mathrm{W}$ hence $I_p = 1.30 > 1$, i.e. we confirm drag reduction.

The upper-bound estimate of the moving body drag is obtained using (4.7), after correcting for the drag of the appendages. Separate experiments established the drag of the mast, after streamlining the lower edge to avoid edge drag. No correction was made for other sources of drag, such as the two smaller fins attached on the body. For the example case the appendage drag was found to be $D_{ap} = 0.435\,\mathrm{N}$, hence
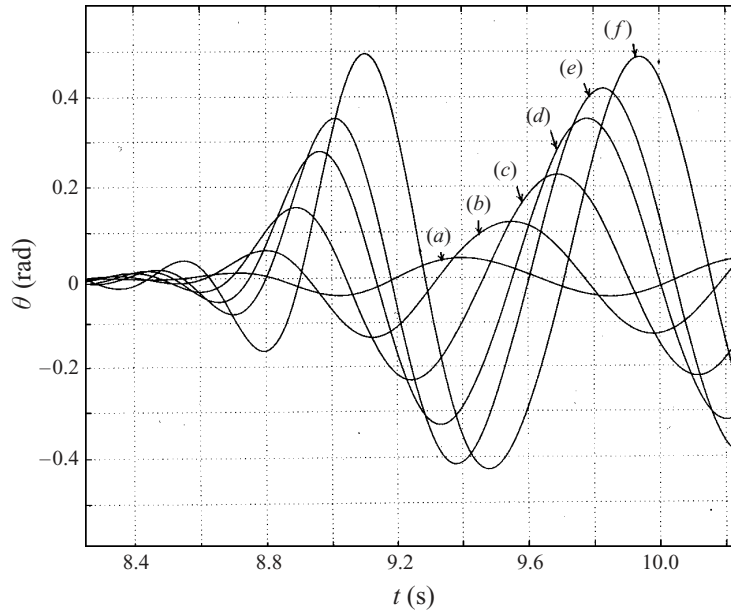
FIGURE 9. Measured motions of links as function of time, including start-up period. (*a*) links 1 and 3; (*b*) link 4; (*c*) link 5; (*d*) link 6; (*e*) link 7; (*f*) link 8 (tail). Second link is rigidly attached to mast; links 1 and 3 move in anti-phase. Non-dimensional parameters: $St = 0.25$, $Re = 800\,000$. Run parameters: $U = 0.7\,\mathrm{m\,s^{-1}}$, $A = 0.16\,\mathrm{m}$, $f = 1.1\,\mathrm{Hz}$, $\lambda = 1.06\,\mathrm{m}$.

the net body drag is $D'_o = D_o - D_{ap} = 1.3\,\mathrm{N}$. The corresponding rigid-body drag coefficient based on the wetted area is $c_{Dw} = 0.009$, which is roughly equal to the drag coefficient on a streamlined body with length to transverse width ratio of about 4: in Hoerner (1965), for a body of revolution with length to diameter ratio equal to 5 in stimulated turbulent flow, a value of about 0.008 is provided. The flow in the present experiments was stimulated to be turbulent, tripped by a ring at the interface between the rigid nose cone and the flexing body, as well as the rough Lycra cloth of the skin structure. The moving-body upper-bound drag estimate, obtained using (4.7), is $D_u = (P_p/U) - T_A - D_{ap} = 0.84\,\mathrm{N}$, i.e. $D_u/D'_o = 0.65$, corresponding to a drag coefficient based on the wetted area of $c_{Dw} = 0.0058$, i.e. a drag reduction of 35%.

We have investigated speeds ranging from 0.5 to $1.0\,\mathrm{m\,s^{-1}}$, which are the speeds allowed by the limits of our current equipment: length of tank, transients time to settle down, capability of the skin structure to support lateral pressure. The results were repeatable within 4% and consistent. Transition to turbulence through stimulation was complete in terms of its effects on the drag coefficient of the rigid body at speeds higher than $0.6\,\mathrm{m\,s^{-1}}$, so a speed of $U = 0.7\,\mathrm{m\,s^{-1}}$ was chosen to investigate the sensitivity of drag reduction to parametric change, since it provided sufficiently long time records for accurate power and drag estimation.

4.5. *Sensitivity to parametric variation*

We provide detailed measurement data for two cases:

(*a*) Figure 11 provides the joint force and velocity measurements, and Figure 12 provides the mast force and total power measurements for Strouhal number 0.198. Table 5(*a*) provides the power used to drive each joint individually. In this case the tail requires small but positive power, and the drag reduction realized is 47.8%.
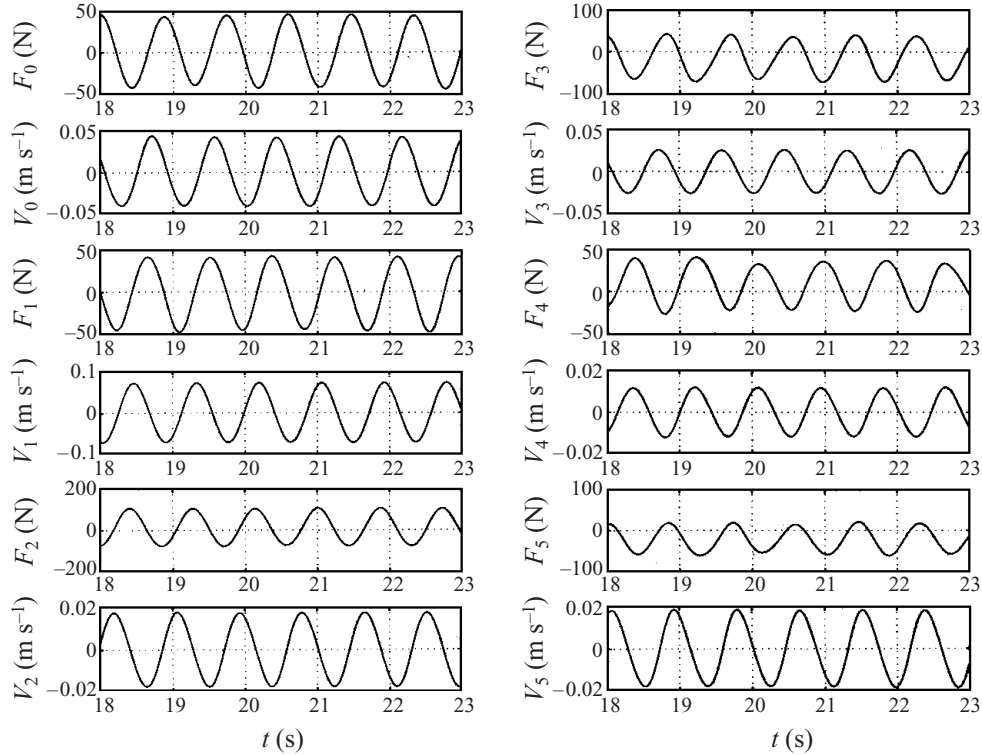
FIGURE 10. Joint force and velocity time records. Non-dimensional parameters: $St = 0.25$, $Re = 800\,000$. Run parameters: $U = 0.7\,\mathrm{m\,s^{-1}}$, $A = 0.16\,\mathrm{m}$, $f = 1.1\,\mathrm{Hz}$, $\lambda = 1.06\,\mathrm{m}$.

(*b*) Figure 13 provides the joint force and velocity measurements, and figure 14 provides the mast force and total power measurements for Strouhal number 0.353. Table 5(*b*) provides the power used to drive each joint individually. In this case the tail requires substantial power. Drag reduction realized is 43.7%.

As shown from the *three* cases above there is strong parametric dependence on the qualitative and quantitative form of the data. We considered five principal parameters: (*a*) Strouhal number, St; (*b*) tail nominal angle of attack, α; (*c*) phase angle at the tail between lateral and angular motions, ψ; (*d*) total lateral excursion of the tail, A; and (*e*) body wavelength, λ.

Over six hundred experiments were conducted, concentrating on parametric combinations where drag reduction was found to be the largest. A subset of these experiments, about three hundred, resulted in conditions of self-propulsion, i.e. zero average mast force. It must be noted that the condition of self-propulsion can only be achieved iteratively, since the drag of a flapping body varies as function of the parameters used. We present in figure 15 these self-propulsion results because of their direct relevance to fish propulsion. We report the *apparent drag reduction* for these experiments as a percent, using the form of (4.9), but substituting in the denominator for D_o the drag of the rigid body alone (i.e. subtracting the appendage drag of the mast and the tail). The true drag reduction is higher since no correction for the hydrodynamic efficiency of the body/tail system is made.

Figure 15 provides experimental results showing the drag reduction, as function of the principal parameters. Five plots are presented in figure 15, each showing the
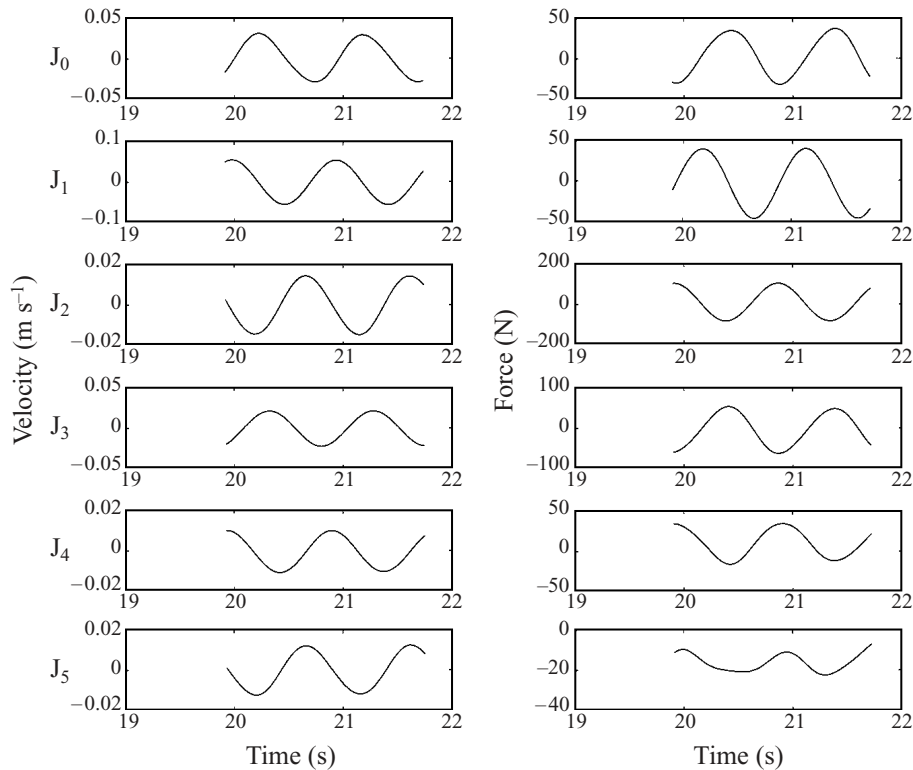
FIGURE 11. Force and velocity time history records for the individual joints.
Run A – $St = 0.198$.

drag reduction realized by varying a single parameter, while holding all other free parameters roughly constant, within 5% of a mean constraint value. These plots represent a small subset of the total database, obtained through optimization of the drag reduction under self-propulsion conditions, using genetic algorithms to reduce the number of experiments needed. The cases exhibiting the largest drag reduction were selected.

For all cases, the swimming speed U was held at $0.7\,\mathrm{m\,s^{-1}}$. The constraints used to study the parametric dependence of the self-propulsion data are described below, and the parametric dependence of the observed drag reduction on the principal parameters is found as follows:

(i) Phase angle at the tail between lateral and angular motions, ψ: values in the range of 80° to 100° degrees provide maximum drag reduction, in agreement with Anderson *et al.* (1998), with a peak around 95°. Constrained parameter values: Strouhal number $St \approx 0.16$; backbone wavelength $\lambda \approx 55$ in.; tail angle of attack $\alpha \approx 15°$.

(ii) Body wavelength, λ: a wavelength comparable to the body length is found to provide maximum drag reduction, in the range of 40 to 60 in. (1 to 1.5 m), with a peak at around 52 in., or roughly 1.1 times the body length. Constrained parameter values: Strouhal number $St \approx 0.16$; phase angle $\psi \approx 92°$; tail angle of attack $\alpha \approx 15°$.

(iii) Tail nominal angle of attack, α: a high angle of attack was found to provide highest drag reduction in most cases, preferably in the range of 15° to 25°. A
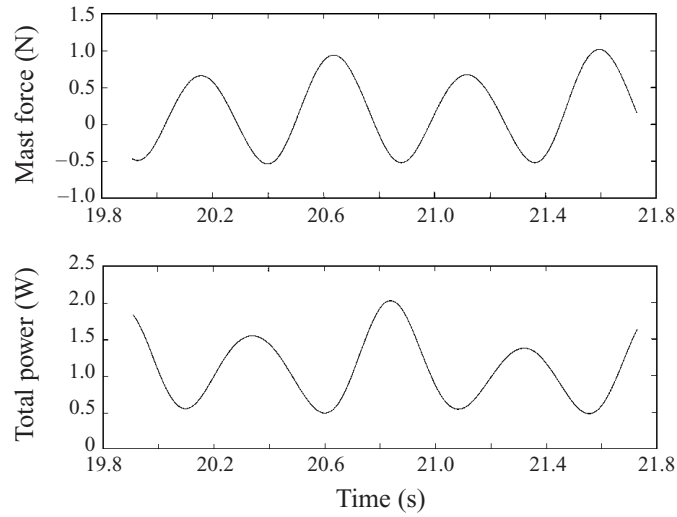
FIGURE 12. Total mast force and total input power time history records.
Mean total input power 1.08 W. Run A – $St = 0.198$.

slight peak is observed at around 17°. Again, this is in agreement with experiments on flapping foils demonstrating high efficiency at angles above 15°, (Anderson *et al.* 1998). Constrained parameter values: Strouhal number $St \approx 0.16$; backbone wavelength $\lambda \approx 55$ in; phase angle $\psi \approx 92°$.

(iv) Total lateral excursion of tail motion, A: drag reduction is relatively insensitive to this parameter for a value higher than about 5 in. (13 cm), although a slight peak is observed at around 4.6 in. or 10% of the total body length. Constrained parameter values: Strouhal number $St \approx 0.16$; backbone wavelength $\lambda \approx 55$ in.; phase angle $\psi \approx 92°$; tail angle of attack $\alpha \approx 15°$.

(v) Strouhal number, St: there are two peaks of maximum drag reduction, one at about $St = 0.16$ and a second at about $St = 0.25$, closely related to peaks in the efficiency of the tail reported in the experiments of Anderson *et al.* (1998). Constrained parameter values: backbone wavelength $\lambda \approx 55$ in.; phase angle $\psi \approx 92°$; tail angle of attack $\alpha \approx 15°$; total lateral excursion of the tail $A \approx 5$ in. .

It should be recalled that the upper estimate of drag given by expression (4.7) attributes hydrodynamic losses to drag; hence in order to observe drag reduction as defined herein, a high propulsive efficiency is also essential. As a result, it is not surprising to find that high drag reduction is observed for parametric values where an oscillating foil is efficient. Vorticity control is a principal mechanism through which flapping foils achieve high efficiency (Anderson *et al.* 1998), and also recover energy from oncoming vortical flow (Gopalkrishnan *et al.* 1994); this is also the reason why the Strouhal number, which governs the dynamics of the shed vorticity, is a principal parameter in the present experiments.

All cases reported to exhibit drag reduction share one common characteristic: the phase speed of the travelling wave imposed on the body was larger than the forward speed. This is the single parametric condition that seems to be exclusively related to achieving drag reduction on the body and is unrelated to wake management. It is important to note that this result is identical with the conclusions of Taneda & Tomonari (1974) who reported turbulence and drag reduction in a two-dimensional elastic sheet placed in uniform flow and undergoing transverse oscillations in the form of a travelling wave.
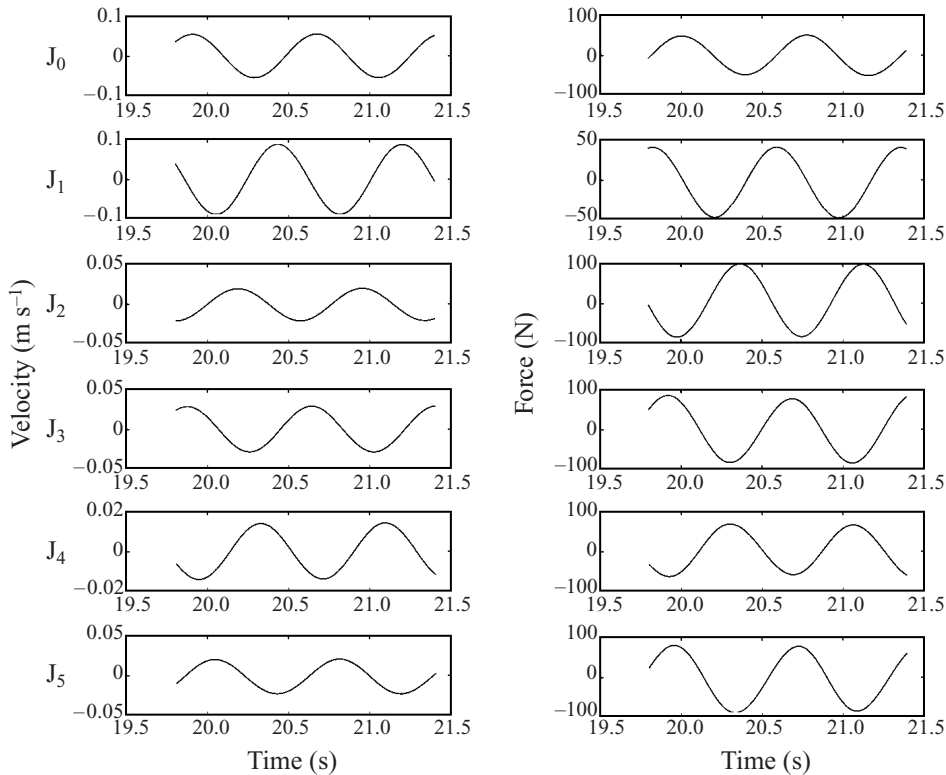
FIGURE 13. Force and velocity time history records for the individual joints.
Run B – $St = 0.353$.

	Run A	Run B
Joint 0	0.1318	0.8848
Joint 1	0.3241	0.470
Joint 2	0.04919	0.1279
Joint 3	0.4551	1.163
Joint 4	0.1160	0.457
Joint 5	0.00324	0.6484

TABLE 5. Mean power (in W) delivered to individual joints. (*a*) Run A – $St = 0.198$,
and (*b*) Run B – $St = 0.353$.

To place the drag reduction of actively swimming flexible bodies in perspective, we estimated the drag coefficient of the main body alone, using the upper estimate expression (4.7); we also subtracted the separately measured drag of the strut and the tail. Figure 16 provides the rigid-body drag coefficient (without the tail) based on the wetted surface, as well as the minimum drag coefficient for an actively swimming body, as function of speed. We show in the same figure the curves representing flat-plate laminar drag as well as laminar and turbulent drag of a streamlined body with length to diameter ratio equal to 5 (Hoerner 1965). For each speed we chose to show the cases with the absolute minimum drag coefficient, and without requiring that the body be self-propelling. Hence the set of data on which figure 16 is based is much larger
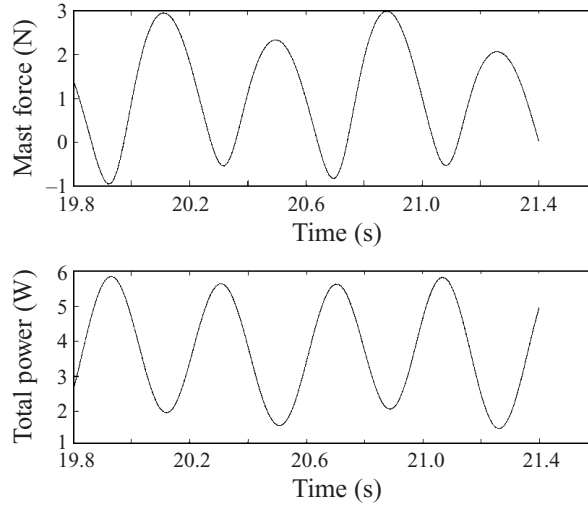
FIGURE 14. Total mast force and total input power time history records. Mean total input power 3.711 W. Run B – $St = 0.353$.

Reynolds number Re		710950	829440	888690	947940
Swimming speed U	(m s^{-1})	0.60	0.70	0.75	0.80
Strouhal number St		0.25	0.30	0.25	0.25
Wavelength λ	(m)	1.22	1.22	1.22	1.22
Tail phase angle ψ	(deg.)	90.0	90.0	90.0	90.0
Tail angle of attack α	(deg.)	13.7	15.4	13.2	12.5
Tail lateral excursion A	(m)	0.152	0.152	0.152	0.152
Drag coefficient		0.00305	0.00330	0.00258	0.00192

TABLE 6. Run parameters for the four minimum-drag cases shown in figure 16.

than the set of data used for figure 15. Whereas maximum drag reduction realized for self-propelled motions is around 50%, the maximum drag reductions realized for thrust-producing cases may exceed 70% in some cases. The run parameters for the minimum drag cases presented in figure 16 are given in table 6.

Figure 16 shows that under optimized conditions the drag coefficient of the body is close to the value corresponding to laminar flow. In addition to plausible laminarization of the flow, the data seem to indicate some form drag reduction as well. But, since in order to estimate the flapping-body drag coefficient we subtract the drag of the tail in its straight position (as part of the appendages), there is a small ambiguity concerning the exact value of the moving drag coefficient and we cannot place confidence in the apparent form drag reduction. Such drag reduction, however, would not be qualitatively different from the reduction achieved by Tokumaru & Dimotakis (1991) for a bluff body.

5. Discussion of drag reduction results

The most plausible conclusion from the force and power data is that the drag reduction is caused by a combination of two mechanisms:
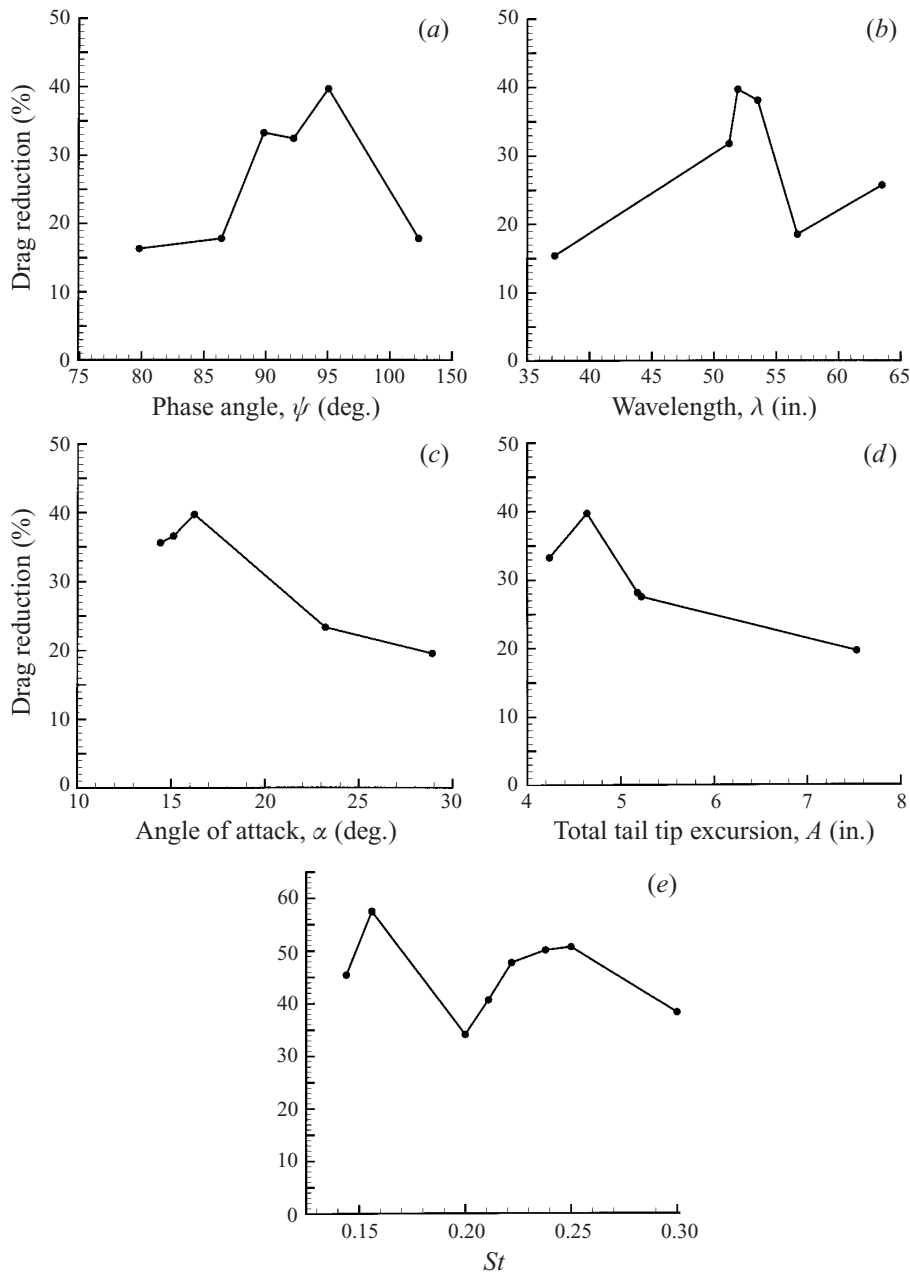
FIGURE 15. Apparent drag reduction as a percent of rigid-body drag under conditions of self-propulsion as a function of the principal parameters: (*a*) tail phase angle ψ; (*b*) backbone wavelength λ; (*c*) tail angle of attack α; (*d*) total tail lateral excursion A; (*e*) Strouhal number St.

(*a*) laminarization of the boundary layer,
(*b*) vorticity control by the tail fin.

Taneda & Tomonari (1974) considered the flow around, and estimated the wall stress on a flexible rectangular sheet placed within an air or water stream of velocity U, undergoing oscillations in the form of a travelling wave. He noted that when
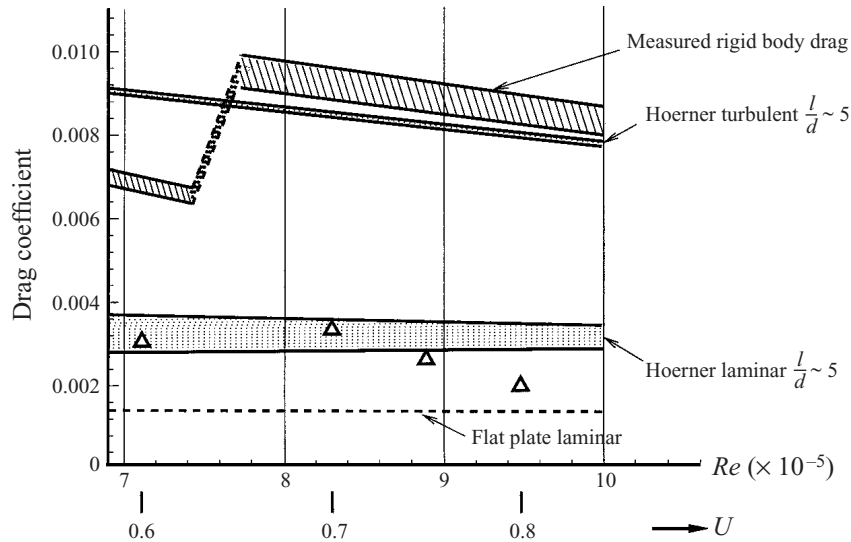
FIGURE 16. Drag coefficient versus speed and corresponding Reynolds number. Values of minimum drag are denoted by △.

the phase speed c_p of the travelling wave exceeded the speed of the external flow, turbulence was suppressed, separation was absent and the wall stress was reduced. Taneda conducted tests up to Reynolds number of 3×10^6, consistently observing progressive turbulence reduction as c_p/U increased.

There are close similarities between Taneda's results and the present experiments despite the three-dimensional form of the body considered herein versus the two-dimensional flexible sheet studied by Taneda. The similarity is not coincidental: flow visualization using digital particle image velocimetry around live fish by Anderson (1996), as well as limited visualization tests around the robotic mechanism described herein, have shown that the flow patterns around the body of the fish, visualized within a plane parallel to the direction of lateral motion, at the mid-height of the body, are qualitatively similar to the two-dimensional patterns predicted for an undulating plate by Wu (1961, 1971): substantial spanwise, body-bound travelling vorticity develops, which is shed by the time it reaches the caudal peduncle, forming large vortices, which are then manipulated by the tail to form a propulsive reverse Kármán street. Quasi-two-dimensional forces around unsteadily flapping three-dimensional plates are also reported in the numerical simulations of Cheng, Zhuang & Tong (1991).

In all cases where substantial drag reduction was observed in our experiments, the phase velocity of the travelling wave exceeded the velocity U, in complete agreement with the experiments of Taneda. Reduction of the overall drag, however, requires additionally that the Strouhal number primarily, and other parameters of the foil to a somewhat lesser degree, must be within optimal, relatively narrow ranges. These additional requirements result from the need to use the tail to control the vorticity generated by the unsteady flapping of the body, shed just prior to the caudal peduncle, as well as operate the flapping tail under optimal conditions (Anderson *et al.* 1998).

The manipulation of body-generated vorticity by the tail in live fish (Anderson 1996) follows the basic trends of vorticity control (Gopalkrishnan *et al.* 1994) and explains the sensitivity of the overall drag reduction to the Strouhal number variation. In fact, for certain parametric combinations outside the optimal range, instead of drag

reduction we observed drag amplification which could become very substantial, up to 300% compared to rigid-body drag. The generation and subsequent manipulation of additional unsteady vorticity appears to be a basic mechanism of flow control in the present experiments, as it was in the wake control experiments of Tokomaru & Dimotakis (1991).

Rome *et al.*(1993) have measured directly the power produced by the muscle of live fish along its length. Their basic conclusion is that the middle and rear part of the fish produce most of the power, while the front produces relatively little. The present power measurements are in agreement with the conclusions of Rome *et al.*: the eight-link structure of the robotic mechanism herein replicates to a certain extent the body structure of live fish, although the latter contains a considerably greater number of vertebrae. From table 5, corresponding to a self-propulsion case, we find that if the vehicle is subdivided longitudinally into three parts of roughly equal length, the front part absorbs about 12%, the middle part 35%, and the rear part 53% of the total input power.

The present results seem also to confirm that fish-like propulsion must be associated with drag reduction, albeit at a lower Reynolds number than for fast fish and dolphins. If drag reduction persists to higher Reynolds numbers, the potential for application is significant. The Reynolds numbers considered in the present experiments are transitional ($Re \approx 10^6$), and turbulence is artificially stimulated. The experiments by Taneda & Tomonari (1974) which reach up to $Re = 3 \times 10^6$, and data for the fastest swimming fishes (Aleyev 1977), indicate that it is possible that the same mechanisms may apply to Reynolds numbers at least as high as 10^7.

6. Computational results

The experimental results suggest that significant reduction in body drag is achievable through fish-like propulsion. The power expended by the motors and the mast force are the principal measured quantities which prove drag reduction. While the mast force is governed by viscous mechanisms, one may expect that, in the absence of large form drag, the power is principally influenced by inviscid mechanisms, and hence could be calculated fairly accurately by inviscid numerical methods, provided the vorticity shed from sharp trailing edges (such as the tail fin) is properly modelled and accounted for. In order to check this hypothesis and hence further elucidate the principal flow mechanisms, we developed an inviscid computational model capable of simulating the flow kinematics and forces around a three-dimensional body under the same conditions as used in the experiments.

We consider a flexible, streamlined body equipped with a sharp-trailing-edge, rigid caudal fin. We study through simulation the problem of this body starting from rest to reach a constant horizontal velocity U while undergoing periodic undulations about its mean line within an inviscid, incompressible fluid. A thin shear layer wake is continuously shed from the trailing edge of the caudal fin as time proceeds. The flow, with the exception of the thin wake, is assumed to be irrotational, allowing the existence of a velocity potential $\phi(x, t)$. All time and length scales are chosen to be non-dimensional with respect to the body length $\ell = 1$ and swimming speed $U = 1$. A three-dimensional numerical panel method based on Green's theorem is employed to find the velocity potential on the body and in the wake. The details of this method are developed in the Appendix.

The surface of a body similar to the robotic mechanism described above is numerically represented by quadrilateral panels. The body, excluding the caudal fin, has $O(2000)$ panels, and the caudal fin is gridded with $O(1000)$ panels. The motion of the

body is prescribed to be identical to that of the flexible, fish-like robot. A backbone wave, as described by (2.1) and (2.2), characterizes the motion applied to the body. The tail follows the path of the caudal peduncle but can be pivoted with oscillatory angular motion of arbitrary amplitude and arbitrary phase angle with respect to the lateral motion, resulting in a nominal angle of attack α. The simulation starts with the body in a flexed position, and the caudal fin wake is shed continuously in time as the fish begins to move. Several periods of the motion are simulated to eliminate transients associated with initial conditions, and to achieve steady-state wake structure, motions and forces. The effects of the initial wake structure on the flow are damped out quickly, and steady-state behaviour of integrated quantities is evident typically after one period of the motion. The time step depends on the Strouhal number and the frequency of the backbone wave, and is typically chosen as $dt = 0.05$. The wake generally contains up to $O(8000)$ panels at the conclusion of the simulation. A typical simulation result is shown in figure 17, where the evolving wake structure is evident. The evolving wake structure behind the fish in figure 17 compares well qualitatively with dye visualization experiments performed in the wake of the flexible robot, such as those illustrated in Triantafyllou & Triantafyllou (1995).

Quantitative comparison between the experimental measurements and the numerical simulations of expended power can be made directly. As mentioned above, the simulations are made for an inviscid fluid and no comparison of forces can be made; however, in the absence of substantial separation or form drag it is expected that the power estimates should be sufficiently close. Geometric differences between the numerical body representation and the flexible robotic mechanism include the omission of the anal and secondary dorsal fin, which were included on the robotic mechanism, and the smaller peduncle region in the numerical model just ahead of the tail connection. Differences in the peduncle contraction region between the numerical and the robotic hull can be assumed to have a small effect on the hydrodynamic similitude between the models, as this region sustains a small hydrodynamic load and serves to transmit force from the oscillating tail to the centre of mass of the body (Lighthill 1975). Also, the effects of upstream vorticity shed by the body on the flow dynamics around the caudal fin are not modelled in this simulation, due to the smooth nature of the synthetic robotic mechanism skin without predetermined separation edges and to the small size of the secondary dorsal or anal fins. These dynamics may be important for other geometric configurations, as vorticity control may account for 5–15% of the recovered energy (Gopalkrishnan *et al.* 1994), and are the subject of ongoing research (Wolfgang 1999).

Input parameters for three experimental runs and corresponding numerical simulations can be found in table 8. The numerical simulations employed 1500 body panels, 1280 tail panels, and produced 40 wake panels per time step for 250 time steps, totalling 10 000 panels at the simulation's conclusion. Again, the time step was chosen to be $dt = 0.05$ with a desingularization radius of $\delta = 0.025$.

Power time histories for both the experimental runs and the numerical simulations can be found in figure 18. For the first pair of records, Run 1, 47.7% drag reduction was experimentally realized at a Strouhal number of 0.182. The data for Run 2 at a Strouhal number of 0.198 and Run 3 at a Strouhal number of 0.353 were described previously in §4.5 where they were called Runs A and B, experimentally achieving drag reductions of 47.8% and 43.8%, respectively. The time records compare well qualitatively, revealing a second harmonic in the time history of the power expended. For all three runs, the numerically computed propulsive efficiency was over 90%.

Quantitative agreement is good under the assumptions made. The exact timing
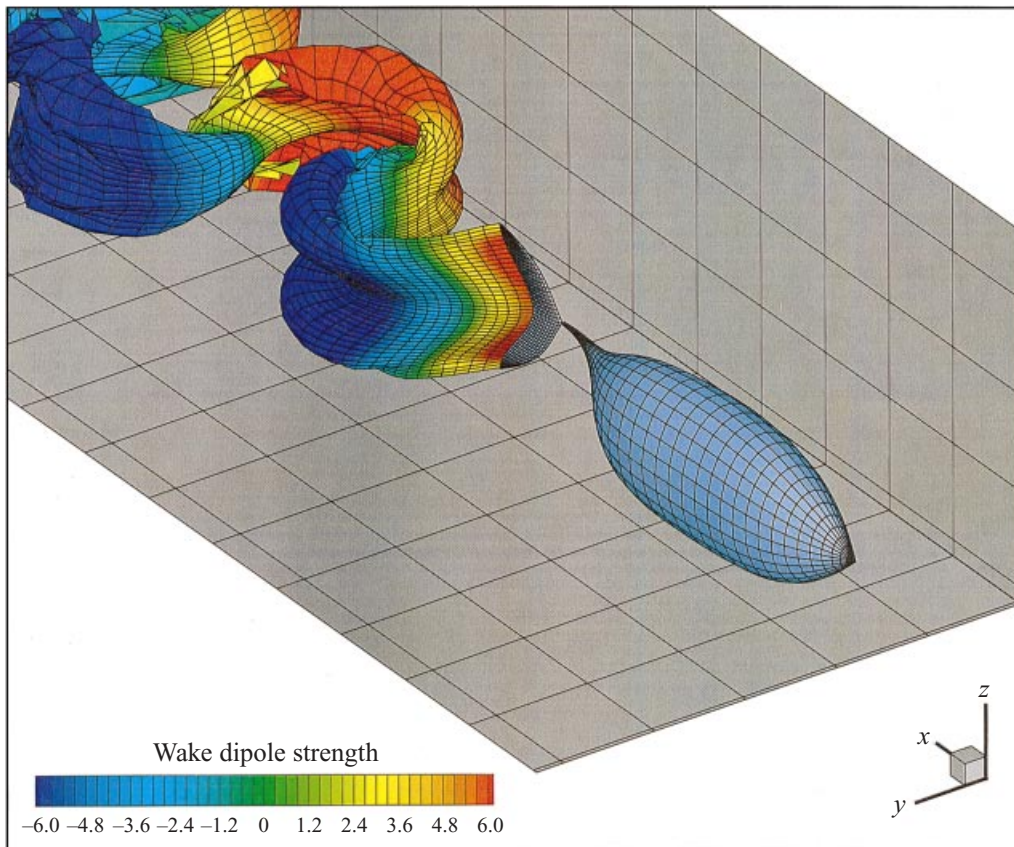
FIGURE 17. Numerical simulation results showing the evolving straight-line swimming wake structure. Strouhal number $St = 0.182$. Run parameters: $U = 0.656$ BL s^{-1}, $\omega = 6.278$ rad s^{-1}, $\lambda = 0.936$ BL, Double tip amplitude $A = 0.120$ BL, $\alpha = 24.8°$, Tail phase $= 80°$.

among the links of the experimental device was found to affect the overall power time record and may be a cause of deviation due to the flexibility of the experimental apparatus. Also, natural resonances in the mechanical system and mechanical losses are expected to cause some deviations between theory and experiment. Despite the simplifications made through the choice of the numeric scheme, and the unmodelled mechanical behaviour and losses, the difference in the mean power between theory and experiment is less than 20% in two of the cases and 7.5% for Run 1.

7. Conclusions

Direct force and power measurements on a streamlined, fish-like, flexible-hull vehicle with turbulence stimulation, show that the drag on the actively swimming body is smaller than the drag on the same body towed straight and rigid. The drag reduction is caused exclusively by the actively controlled transverse motion.

The maximum drag reduction recorded was in excess of 70%, at Reynolds number 10^6. Drag reduction is particularly sensitive to two parameters: (a) the speed of the travelling wave over the body, c_p, must exceed the speed of travel U; and (b) the Strouhal number must be within a range which varies with the specific thrust developed and lies between $St = 0.12$ and 0.35. In addition, the flapping foil
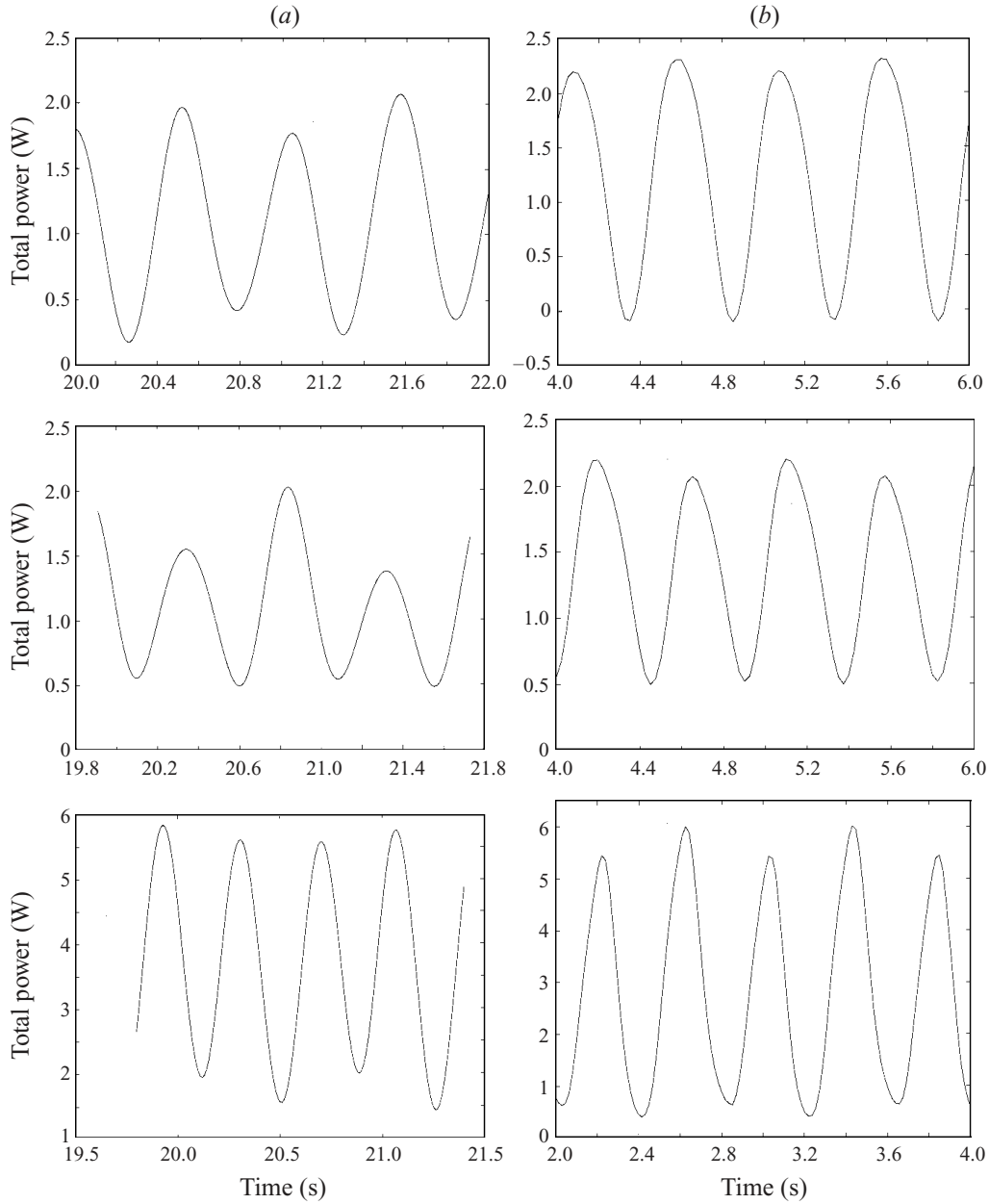
FIGURE 18. Total power into the fluid for straight-line swimming. The mean power deviation between (*a*) the experimental and (*b*) the numerical time history power records is for Run 1: 7.48%, for Run 2: 19.4%, and for Run 3: 17.8%.

parameters must be selected for optimal hydrodynamic efficiency, i.e. angle of attack between 14° and 25°, phase angle between lateral motion and angular motion in the range between 70° and 110°, and high amplitude-to-chord ratio.

Numerical simulations were performed with an inviscid numeric scheme employing a boundary-integral formulation for arbitrary body geometry and motions, with desingularized infinitesimal wake sheet representation to model the nonlinear dynam-

		Run 1	Run 2	Run 3
Strouhal number St	(–)	0.182	0.198	0.353
Swimming speed U	$(\mathrm{BL\,s^{-1}})$	0.656	0.656	0.656
Tail circular frequency ω	$(\mathrm{rad\,s^{-1}})$	6.278	6.830	7.767
Wavelength λ	(BL)	0.936	0.936	1.321
Tip double amplitude A	(BL)	0.120	0.120	0.187
Angle of attack α	(deg.)	24.8	19.0	19.0
Tail phase between pitch and heave	(deg.)	80.0	97.7	97.7
Drag reduction (experiment)	(%)	47.7	47.8	43.8
Mean power input (experiment)	(W)	1.07	1.08	3.71
Mean power input (computation)	(W)	1.15	1.29	3.05
Mean power input difference	(exp. vs. comp.)	7.48%	19.4%	17.8%

TABLE 7. Parameters for three cases for comparison between experimental results and numerical simulations. BL = body length.

ics of the wake vorticity. The numerical model was validated through systematic convergence tests. Its predictions for the power expended by a body moving forward at constant speed and oscillating transversely similarly to the experimental apparatus were in good qualitative and quantitative agreement with experimental measurements.

Based on the quantitative estimates of drag reduction, and the importance of the Strouhal number, as well as vorticity control observed in live fish (Anderson 1996), we propose as a plausible mechanism for drag reduction the combination of two mechanisms of flow control:

(i) laminarization of the boundary layer as a result of body flexing in the form of a travelling wave with $c_p > U$,

(ii) vorticity control by the tail, which manipulates body–shed vorticity to create a propulsive reverse Kármán street.

Within the parametric range considered, we find that drag reduction increases with Reynolds number. This may be of great significance for applications.

Appendix. Numerical method description

Herein we formulate the numerical method used to simulate the motion of a three-dimensional, streamlined, flexible body with arbitrary geometry and nonlinear wake sheet evolution.

The computational domain is enclosed by three surfaces: the body surface S_b, the shear layer wake S_w, and the far-field boundary S_∞. Laplace's equation for the velocity potential $\phi(\boldsymbol{x}, t)$ in the fluid domain governs the conservation of mass. Further, we can describe the total velocity potential $\phi(\boldsymbol{x}, t)$ as the linear superposition of the body perturbation velocity potential $\phi_b(\boldsymbol{x}, t)$ and the wake perturbation velocity potential

		dt = 0.2	dt = 0.1	dt = 0.05
k		400	400	400
δ_w	(1/c)	0.05	0.05	0.05
α	(deg.)	10	10	10
C_L	(computation)	0.8099	0.8149	0.8256
C_L	(Hoerner)	0.862	0.862	0.862
Error	(%)	6.04	5.46	4.22

TABLE 8. Convergence of the numerical method for decreasing time step dt. NACA 0012 foil section with aspect ratio $AR = 12$.

		k = 100	k = 200	k = 400	k = 800
dt		0.1	0.1	0.1	0.1
δ_w	(1/c)	0.05	0.05	0.05	0.05
α	(deg.)	10	10	10	10
C_L	(computation)	0.6001	0.7761	0.8149	0.8441
C_L	(Hoerner)	0.862	0.862	0.862	0.862
Error	(%)	30.4	9.97	5.46	2.08

TABLE 9. Convergence of the numerical method for increasing panel number k. NACA 0012 foil section with aspect ratio $AR = 12$.

$\phi_w(\boldsymbol{x}, t)$. We formulate the boundary value problem for the body perturbation velocity potential $\phi_b(\boldsymbol{x}, t)$, as the strength of the wake is known $\phi_w(\boldsymbol{x}, t)$. A prescribed body motion $\boldsymbol{V}_{body}$ gives the Neumann body boundary condition in terms of the body perturbation potential and the body normal $\hat{\boldsymbol{n}}_B$:

$$\frac{\partial \phi_b(\boldsymbol{x}, t)}{\partial n_b} = (\boldsymbol{V}_{body}(\boldsymbol{x}, t) - \nabla\phi_w(\boldsymbol{x}, t)) \cdot \hat{\boldsymbol{n}}_B(\boldsymbol{x}, t). \tag{A 1}$$

An unsteady Kutta condition is applied to enforce smooth flow leaving the trailing edge. At any time we set the strength of the shed wake potential to the jump in the body perturbation potential between the upper and lower surfaces near the trailing edge (TE):

$$\Delta\phi_b(\boldsymbol{x}, t)|_{TE} = \phi_w(\boldsymbol{x}, t)|_{TE}. \tag{A 2}$$

Green's theorem allows the body perturbation velocity potential $\phi_b(\boldsymbol{x}, t)$ to be described by a source-dipole distribution over the body surface S_B, and the wake perturbation velocity $\phi_w(\boldsymbol{x}, t)$ potential by a dipole distribution over the wake surface S_W. The influence of the far-field boundary S_∞ decays in proportion to the inverse of the distance from the body, and thus the body perturbation potential $\phi_b(\boldsymbol{x}, t)$ can be written in terms of integrals over the body and wake surface of the influence of the source and dipole distributions.

We discretize the body into constant-strength quadrilateral source-dipole panels, and we represent the unsteady, variable-strength wake by constant-strength quadrilateral dipole panels, equivalent to an infinitesimal vortex sheet. The system of equations which results for the body perturbation potential distribution is solved using an iterative scheme. While the number of body panels is constant, the number of wake panels increases in time, as a wake of time-varying strength is continuously shed from

		$\delta_w = 0.1$	$\delta_w = 0.05$	$\delta_w = 0.025$	$\delta_w = 0.01$
k		400	400	400	400
dt		0.1	0.1	0.1	0.1
α	(deg.)	10	10	10	10
C_L	(computation)	0.8141	0.8149	0.8152	0.8153
C_L	(Hoerner)	0.862	0.862	0.862	0.862
Error	(%)	5.56	5.46	5.43	5.42

TABLE 10. Convergence of the numerical method for decreasing δ_w. NACA 0012 foil section with aspect ratio $AR = 12$.

the trailing edge. This numeric scheme is temporally integrated using a fourth-order Runge–Kutta scheme.

Although problems dealing with an infinitesimally thin vortex sheet are not well-posed because the rate of growth of Kelvin–Helmholtz instability increases with the wavenumber of the disturbance, the problem can be dealt with numerically by introducing some artificial damping, which removes the singularity from the problem (Krasny 1986). Without this filtering, numerical instabilities resulting from the ill-posedness of the singular vortex sheet description rapidly induce simulation breakdown or result in non-physical dynamic growth of the solution, whereas in real flows, viscosity removes the singularity from the flow at all Reynolds numbers. A low-order filtering as described by Krasny (1986) is used to desingularize the wake and body panels, with arbitrary desingularization radii δ_b and δ_w.

The unsteady code was validated by simulating impulsively started motion of a finite-aspect-ratio foil at a small angle of attack to a speed U, in a fluid otherwise at rest. Convergence of the numerical method was confirmed by varying the time step size dt and the number of panels k around the foil, in addition to the aspect ratio AR and the desingularization parameter δ_w for the wake, and comparing the steady lift coefficient to the experimental values illustrated in figure 17-5 of Hoerner (1985). Sample convergence results are given in tables 8, 9, and 10. Simulations were run to a non-dimensional time $Ut/c = 40.0$ for a chord length c.

REFERENCES

ALEYEV, Y. 1977 *Nekton*. W. Junk: The Netherlands.

ANDERSON, J. M. 1996 Vortex control for efficient propulsion. PhD thesis, Joint Program, Massachusetts Institute of Technology & Woods Hole Oceanographic Institution.

ANDERSON, J. M., STREITLIEN, K., BARRETT, D. S. & TRIANTAFYLLOU, M. S. 1998 Oscillating foils of high propulsive efficiency. *J. Fluid Mech.* **360**, 41–72.

BARRETT, D. S. 1996 Forces and efficiency of a flexible hull vehicle. PhD thesis, Massachusetts Institute of Technology.

BARRETT, D. S. & TRIANTAFYLLOU, M. S. 1995 The design of a flexible hull undersea vehicle propelled by an oscillating foil. *9th Intl Symp. on Unmanned Untethered Submersible Technology.*

BEAL, D. N. 1999 Closed-loop vorticity control in fish-like propulsion. PhD thesis, in progress, Massachusetts Institute of Technology.

CHENG, J. Y., ZHUANG, L. X. & TONG, B. G. 1991 Analysis of swimming three-dimensional waving plates. *J. Fluid Mech.* **232**, 341–355.

FFOWCS WILLIAMS, J. E. & ZHAO, B. C. 1989 The active control of vortex shedding. *J. Fluids Struct.* **3**, 115–122.

FIERSTINE, H. L. & WALTERS, V. 1968 Studies in locomotion and anatomy of scombroid fishes. *Mem. Soc. South. Calif. Acad. Sci.* **6**, 1–31.

GOPALKRISHNAN, R., TRIANTAFYLLOU, M. S., TRIANTAFYLLOU, G. S. & BARRETT, D. S. 1994 Active vorticity control in a shear flow using a flapping foil. *J. Fluid Mech.* **274**, 1–21.

GRAY, J. 1936 Studies in animal locomotion VI: The propulsive powers of the dolphin. *J. Expl Biol.* **13**, 192–199.

GURSUL, I. & HO, C. M. 1992 High aerodynamic loads on an airfoil submerged in an unsteady stream. *AIAA J.* **30**, 1117–1119.

HARPER, D. G. & BLAKE, R. W. 1990 Fast-start performance of rainbow trout (*Salmo gairdneri*) and Northern Pike (*Esox Lucius*). *J. Expl Biol.* **150**, 321–342.

HOERNER, S. F. 1965 *Fluid-Dynamic Drag.* Published by the author, N.J.

HOERNER, S. F. 1985 *Fluid-Dynamic Lift.* Hoerner Fluid Dynamics, Vancouver, WA.

KOOCHESFAHANI, M. M. & DIMOTAKIS, P. 1988 A cancellation experiment in a forced turbulent shear layer. *AIAA Paper 88-3713P.*

KRASNY, R. 1986 Desingularization of periodic vortex sheet roll-up. *J. Comput. Phys.* **65**, 292–313.

LIGHTHILL, J. 1975 *Mathematical Biofluiddynamics.* SIAM: Philadelphia.

ROBERTS, F. A. & ROSHKO, A. 1985 Effects of periodic forcing on mixing in turbulent shear layers and wakes. *AIAA Paper 85-0570.*

ROME, L. C., SWANK, D. & CORDA, D. 1993 How fish power swimming. *Science* **261**, 340–343.

TANEDA, S. & TOMONARI, Y. 1974 An experiment on the flow around a waving plate. *J. Phys. Soc. Japan* **36**, 1683–1689.

TANEDA, S. 1978 Visual observations of the flow past a circular cylinder performing a rotary oscillation. *J. Phys. Soc. Japan* **45**, 1038–1043.

TOKOMARU, P. T. & DIMOTAKIS, P. E. 1991 Rotary oscillation control of a cylinder wake. *J. Fluid Mech.* **224**, 77–90.

TRIANTAFYLLOU, M. S. & TRIANTAFYLLOU, G. S. 1995 An efficient swimming machine. *Sci. Am.* **272** (3), 64–70.

TRIANTAFYLLOU, M. S., TRIANTAFYLLOU, G. S. & GOPALKRISHNAN, R. 1991 Wake mechanics for thrust generation in oscillating foils. *Phys. Fluids* A **3**, 2835–2837.

TRIANTAFYLLOU, G. S., TRIANTAFYLLOU, M. S. & GROSENBAUGH, M. A. 1993 Optimal thrust development in oscillating foils with application to fish propulsion. *J. Fluids Struct.* **7**, 205–224.

WOLFGANG, M. J. 1999 Hydrodynamics of flexible-body swimming motions. PhD thesis, Massachusetts Institute of Technology.

WU, T. Y. 1961 Swimming of a waving plate. *J. Fluid Mech.* **10**, 321–344.

WU, T. Y. 1971 Hydromechanics of swimming propulsion. Part 1. Swimming of a two dimensional flexible plate at variable forward speeds in an inviscid fluid. *J. Fluid Mech.* **46**, 337–355.